Evaporation of binary liquids from a capillary tube

Lijun Thayyil Raju[1]†, Christian Diddens[1], Javier Rodríguez-Rodríguez[2], Marjolein N. van der Linden[1,3], Xuehua Zhang[1,4], Detlef Lohse[1,5]‡, and Uddalok Sen[1]¶

[1]Physics of Fluids Group, Max Planck Center Twente for Complex Fluid Dynamics, Department of Science and Technology, and J. M. Burgers Centre for Fluid Dynamics, University of Twente, P. O. Box 217, 7500 AE Enschede, The Netherlands

[2]Departmento de Ingeniería Térmica y de Fluidos, Gregorio Millán Institute for Fluid Dynamics, Nanoscience and Industrial Mathematics, Universidad Carlos III de Madrid, 28911 Leganes, Spain

[3]Canon Production Printing B. V., 5900 MA Venlo, The Netherlands

[4]Department of Chemical and Materials Engineering, University of Alberta, Edmonton T6G1H9, Alberta, Canada

[5]Max Planck Institute for Dynamics and Self-Organization, Am Fassberg 17, 37077 Göttingen, Germany

(Received xx; revised xx; accepted xx)

Evaporation of multi-component liquid mixtures in confined geometries, such as capillaries, is crucial in applications such as microfluidics, two-phase cooling devices, and inkjet printing. Predicting the behaviour of such systems becomes challenging because evaporation triggers complex spatio-temporal changes in the composition of the mixture. These changes in composition, in turn, affect evaporation. In the present work, we study the evaporation of aqueous glycerol solutions contained as a liquid column in a capillary tube. Experiments and one-dimensional simulations show three evaporation regimes characterised by different time evolutions of the normalised mass transfer rate (or Sherwood number, Sh), namely $Sh(\tilde{t}) = 1$, $Sh \sim 1/\sqrt{\tilde{t}}$, and $Sh \sim \exp\left(-\tilde{t}\right)$. Here $\tilde{t}$ is a normalised time. We present a simplistic analytical model which shows that the evaporation dynamics can be expressed by the classical relation $Sh = \exp\left(\tilde{t}\right) \mathrm{erfc}\left(\sqrt{\tilde{t}}\right)$. For small and medium $\tilde{t}$, this expression results in the first and second of the three observed scaling regimes, respectively. This analytical model is formulated in the limit of pure diffusion and when the penetration depth $\delta(t)$ of the diffusion front is much smaller than the length $L(t)$ of the liquid column. When $\delta \approx L$, finite length effects lead to $Sh \sim \exp\left(-\tilde{t}\right)$, i.e. the third regime. Finally, we extend our analytical model to incorporate the effect of advection and determine the conditions under which this effect is important. Our results provide fundamental insight into the physics of selective evaporation from a multi-component liquid column.

Key words:

† Email address for correspondence: l.thayyilraju@utwente.nl
‡ Email address for correspondence: d.lohse@utwente.nl
¶ Email address for correspondence: u.sen@utwente.nl

1. Introduction

Evaporation of multicomponent volatile liquids into a gaseous phase is ubiquitous in both biological and industrial processes (Erbil 2012; Lohse & Zhang 2020; Bourouiba 2021; Morris *et al.* 2021; Lohse 2022). A multicomponent liquid can consist of multiple solvents, surfactants, polymers, colloids, and salts. Evaporation from such systems lead to a plethora of phenomena such as instabilities (Li *et al.* 2020), phase separation (Tan *et al.* 2016), crystallisation (Shahidzadeh-Bonn *et al.* 2008) and evaporation-driven flows (Deegan *et al.* 1997; Hu & Larson 2006). In addition to the composition of the liquid, the geometrical confinement also affects evaporation significantly. The geometrical confinement can be a droplet (Picknett & Bexon 1977; Lohse & Zhang 2020), a liquid film (Okazaki *et al.* 1974), a porous membrane (Prat 2002), a shallow pit (D'Ambrosio *et al.* 2021), or a capillary (Chauvet *et al.* 2009).

Understanding the evaporation of liquids from capillaries is crucial for applications such as microfluidics (Zimmermann *et al.* 2005; Bacchin *et al.* 2022), inkjet printing (Lohse 2022; Rump *et al.* 2022), heat pipes (Chen *et al.* 2016), chromatography (Kamp *et al.* 2005), and the measurement of material properties (Roger *et al.* 2018; Nguyen *et al.* 2022; Merhi *et al.* 2022). Capillaries are also taken as idealised system for modelling porous structures (Yiotis *et al.* 2007; Chauvet *et al.* 2009; Chen *et al.* 2022), the transport of water across skin (Roger *et al.* 2016; Sparr & Wennerström 2000), and film drying (Guerrier *et al.* 1998; Salmon *et al.* 2017).

Capillary evaporation is mainly determined by the behaviour of the volatile liquid meniscus. There have been several experimental and numerical studies to determine the evaporation from a liquid meniscus. These studies describe the evaporation rate (Wayner JR. & Coccio 1971), heat transfer coefficients (Wayner *et al.* 1976; Park & Lee 2003; Dhavaleswarapu *et al.* 2012; Zhou *et al.* 2018), shape of the meniscus (Potash & Wayner 1972; Swanson & Herdt 1992), capillary flows that replenish the evaporated liquid (Potash & Wayner 1972; Ransohoff & Radke 1988; Park & Lee 2003), and additional flows that might be driven by evaporation-induced surface tension gradients (Schmidt & Chung 1992; Buffone & Sefiane 2003; Dhavaleswarapu *et al.* 2007; Cecere *et al.* 2014) or buoyancy (Dhavaleswarapu *et al.* 2007; Buffone 2019).

Broadly speaking, the evaporation of a single-component liquid from a capillary can be divided into two main classes depending on the location of the liquid-air meniscus with respect to the open end of the capillary (henceforth referred to as its 'mouth', see figure 1a). In the first class of problems, the liquid-air interface is far away from the mouth of the capillary. In such a configuration, the evaporation rate is limited by the transport of vapour from the liquid-air interface to the mouth of the capillary tube and it varies approximately as $1/\sqrt{t}$ (Stefan 1873, 1889).

In the second class of problems, the liquid meniscus is at (or relatively close to) the mouth of the capillary (Chauvet *et al.* 2009; Gazzola *et al.* 2009). Within this second class of problems, if the contact angle inside the liquid between the liquid-gas interface and the capillary wall is $\theta \geqslant 90°$, one can immediately realise the resemblance to a sessile droplet (figure 1b). In such a case, one can use the Popov model (Popov 2005; Li *et al.* 2019) to predict the evaporation rate. For $130° > \theta \geqslant 90°$ (which is equivalent to a contact angle $40° > \theta_{\mathrm{drop}} \geqslant 0°$ in the case of a sessile droplet), the evaporation rates will be practically independent of the contact angle (Sobac & Brutin 2011), and mainly depend on the base-radius, ambient humidity, and the properties of the liquid.

However, when $\theta \leqslant 90°$, the droplet-model for evaporation is no longer applicable (figure 1c). The evaporation under such conditions shows two distinct regimes – a "constant rate period" and a "falling rate period" (Chauvet *et al.* 2009; Keita *et al.* 2014,

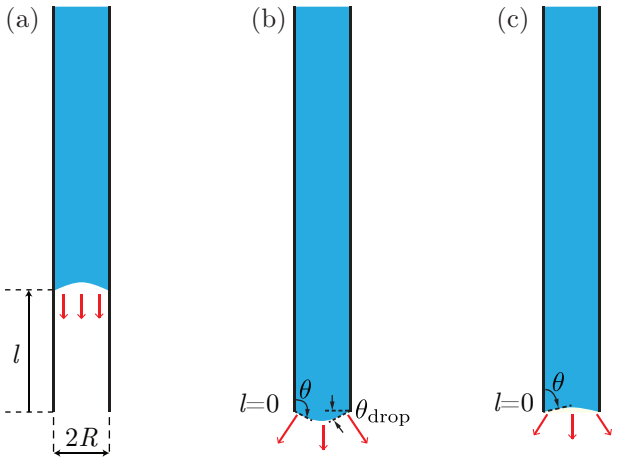

FIGURE 1. Schematic of the different configurations of evaporation from a capillary. (a) First class of problems, where the liquid meniscus is away from the mouth of the capillary ($l >> 0$). (b, c) Second class of problems where the liquid meniscus is close to the mouth of the capillary ($l \approx 0$), with (b) $\theta > 90°$ and (c) $\theta < 90°$. Red arrows represent evaporation flux.

2016) – similar to that observed in the drying of a porous medium (Coussot 2000). During the constant rate period, evaporation is still mainly determined by the ambient conditions. To replenish the liquid lost by evaporation, upstream liquid is driven by capillary pressure to the mouth of the capillary through thin liquid films (Ransohoff & Radke 1988; Chauvet *et al.* 2010). However, even during the so-called constant rate period, the evaporation rate decreases slightly (Coussot 2000; Chauvet *et al.* 2009). For square capillaries, this slight decrease is due to the thinning of liquid films at the mouth of the capillary (Chauvet *et al.* 2009). As evaporation proceeds further, the depinning of the liquid films from the mouth of the capillary leads to the falling rate period (Chauvet *et al.* 2009). When the liquid meniscus is sufficiently far away from the mouth of the capillary, the situation reverts to the first class of problems (figure 1a).

In addition to the studies on evaporation of single-component liquids from capillaries, there have also been several studies on evaporation of multi-component systems, such as evaporation of binary liquid mixtures (Duursma *et al.* 2008; Cecere *et al.* 2014; Salmon *et al.* 2017; Zhou *et al.* 2018), surfactant solutions (He *et al.* 2015; Roger *et al.* 2016, 2018), salt solutions (Camassel *et al.* 2005; Naillon *et al.* 2015), and colloidal dispersions (Abkarian *et al.* 2004; Kamp *et al.* 2005; Sarkar & Tirumkudulu 2009; Wang *et al.* 2020; Roger & Crassous 2021) in capillaries. In all these scenarios, evaporation leads to spatio-temporal variations in the composition of the mixture. Nevertheless, it is generally possible to model the capillary evaporation of a multi-component system as a one-dimensional transport problem. Unsurprisingly, but perhaps interesting to note is that in the absence of instabilities (De Gennes 2001), the one-dimensional model of evaporation of polymeric liquid films (Okazaki *et al.* 1974; Guerrier *et al.* 1998; Saure *et al.* 1998; Okuzono *et al.* 2006) is mathematically-equivalent to the evaporation of binary solutions from capillaries (Salmon *et al.* 2017).

In multi-component systems, especially binary systems, the evaporation rate can also show a constant rate period followed by a falling rate period (Okazaki *et al.* 1974; Salmon *et al.* 2017), similar to pure liquids. However, in multi-component systems, the

different evaporation regimes are additionally determined by changes in the composition of the mixture. Hence, a complete evaporation model must include the spatio-temporal variations in the composition and properties of the mixture. Recently, Salmon *et al.* (2017) showed how a steep decrease in thermodynamic activity and diffusion coefficient of water at high solute concentrations can lead to evaporation being almost independent of ambient humidity for certain molecularly complex fluids. These authors modelled the variable diffusion coefficient as a piece-wise constant function, but bypassed the necessity of using an analytical expression for the thermodynamic activity of water. Moreover, Salmon *et al.* (2017) considered the parameter range where the medium can be approximated as semi-infinite.

In this work, we study the evaporation of binary liquids in capillaries with experiments, direct numerical simulations, and analytical modelling. We perform experiments for the evaporation of glycerol-water mixtures in a cylindrical capillary tube under controlled humidity conditions. Our direct numerical simulations show excellent agreement with the experiments. Further, to unravel the physics of the evaporation dynamics, we develop a one-dimensional analytical model. We introduce a linear approximation for the thermodynamic activity of water as a function of its weight fraction. We also model the condition when the semi-infinite assumption breaks down. Finally, we discuss the explicit role of the advective mass transport compared to the diffusive mass transfer for our particular system. We show that our model accurately predicts the relevant scaling laws observed in the experiments and the numerical simulations.

The paper is organised as follows: in § 2 we describe the experimental setup and observations. The governing equations of our system and the numerical method are described in § 3. In § 4, we provide three simplified analytical models of the problem, each with an added level of complexity over its predecessor, and compare their predictions with the results obtained from the experiments and the simulations. The manuscript culminates with a summary of the results and an outlook in § 5.

2. Experiments

2.1. *Experimental setup*

Aqueous solutions of different mass fractions of glycerol (Sigma-Aldrich) were used as the probe liquids in the present experiments. The reader is referred to Sen *et al.* (2022) for details of the preparation procedure of the liquids and their characterisation. The use of glycerol has the following advantages. First, since glycerol has very low vapour pressure, it is practically non-volatile under current experimental conditions. Thus we only need to account for the evaporation of water. Furthermore, since the more-volatile liquid (water) has higher surface tension, evaporation of water should not lead to any flow instabilities close to the interface (Diddens 2017). Such instabilities occur whenever the mass transfer (evaporation or condensation) leads to an increase in surface tension, such as for evaporating water-ethanol mixtures (Christy *et al.* 2011; Bennacer & Sefiane 2014; Diddens *et al.* 2017; Lopez de la Cruz *et al.* 2021) or condensation of water onto a water-glycerol droplet (Shin *et al.* 2016; Diddens 2017). A more detailed explanation of such instabilities can be found in Diddens (2017).

In the present experiments, we studied the evaporation dynamics of aqueous solutions of glycerol in a thin cylindrical capillary tube (figure 2; inner diameter = 1 mm, outer diameter = 1.2 mm; length = 100 mm, Round Boro Tubing, CM Scientific). The liquid column inside the capillary had an initial height of 19 ± 2 mm. The initial weight fraction of water, w_i, in the water-glycerol mixture was varied as 0.2, 0.6, 0.9, and

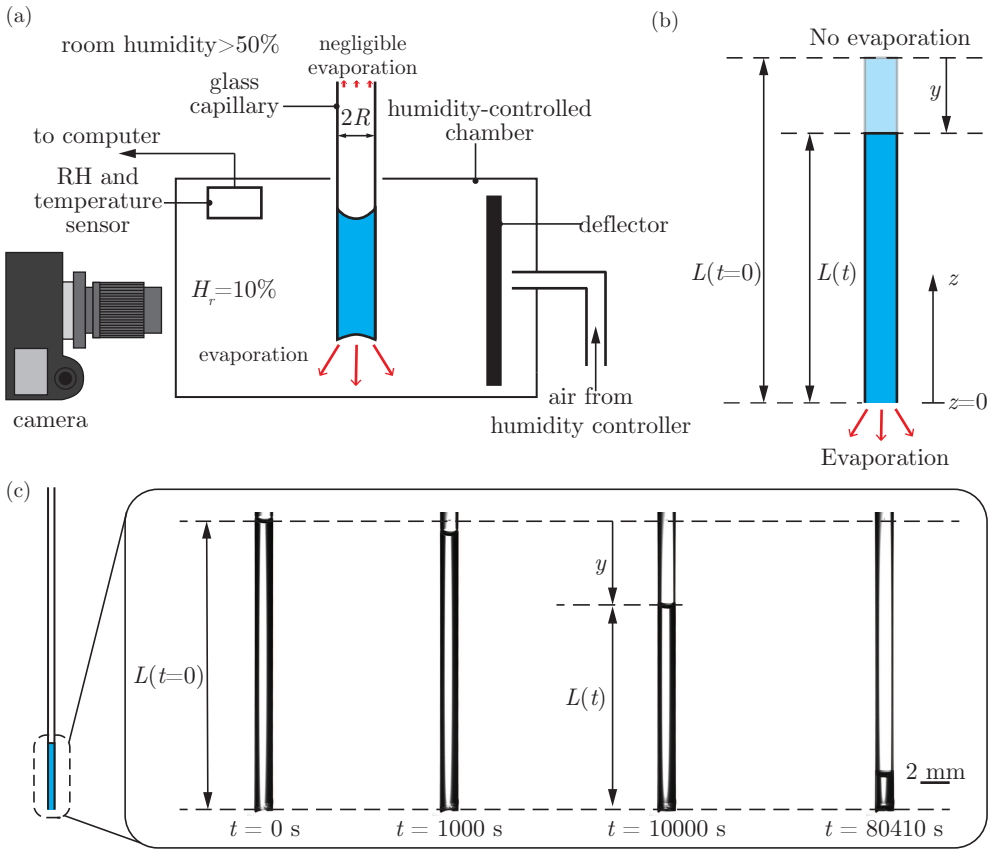

FIGURE 2. (a) Schematic of the experimental setup. (b) Geometry used for numerical simulation and analytical modelling. (c) Left: schematic of the relative length of the liquid column with respect to the length of the capillary; right: time-lapsed experimental snapshots of water-glycerol mixtures in the capillaries for initial weight fraction of water $w_i = 0.9$. The top interface of the liquid mixture keeps moving downwards due to the evaporation of water from the bottom of the capillary. Red arrows represent evaporation flux.

1.0, to cover a wide range of initial compositions. The lower end of the capillary was placed inside an in-house developed, optically-transparent humidity-controlled chamber at room temperature. The humidity and temperature inside the chamber were monitored using a temperature-humidity sensor (HIH6121, Honeywell). The relative humidity in the chamber was maintained at $H_r = 10 \pm 5\%$. The upper end of the capillary tube was exposed to room humidity ($> 50\%$). The evaporation or condensation of water at the upper meniscus was negligible compared to the evaporation from the bottom. This is because of the large distance between the liquid's upper meniscus and the capillary's upper end (see appendix A for a detailed discussion).

The contact line of the lower meniscus remained pinned at the lower mouth of the capillary. Thus, the loss of water by evaporation from the lower mouth of the capillary leads to a decrease in the length L of the liquid column (figure 2c). To study this evaporation process quantitatively, time-lapsed images of the liquid column were captured using a DSLR camera (D750, Nikon) equipped with either a long-distance microscope (Navitar 12×) or a macro lens (50 mm DG Macro D, Sigma), while the capillary tube was

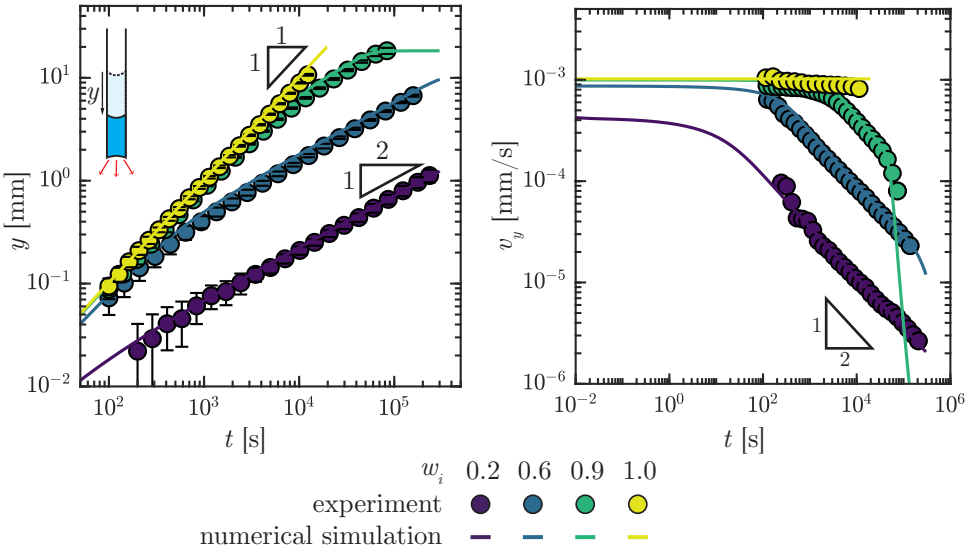

FIGURE 3. (a) Displacement y and (b) velocity v_y of the top interface of the aqueous solutions of glycerol observed in experiments (discrete datapoints) and numerical simulations (continuous lines), for initial weight fractions of water $w_i = 0.2$, 0.6, 0.9, and 1.0.

back-illuminated with a cold LED light source (Thorlabs). For pure water, the velocity v_y of the upper interface,

$$v_y = \frac{\mathrm{d}y}{\mathrm{d}t} = \frac{1}{\rho_w}\frac{\mathrm{d}M''}{\mathrm{d}t}, \tag{2.1}$$

is a direct measure of the evaporation rate $\mathrm{d}M''/\mathrm{d}t$ of water, where y is the displacement of the top interface, M'' denotes the mass per unit area and ρ_w is the density of water.

At a later time, the contact line of the lower liquid meniscus eventually depins. At this point, we stop the measurements because v_y is thereafter no longer a correct measure of the evaporation rate. Additionally, as the lower interface moves inwards into the capillary tube after depinning, the evaporation boundary condition at the lower interface also changes (see § 3.1 for details of the boundary conditions).

2.2. *Experimental results*

The discrete datapoints in figure 3a denote the experimentally obtained vertical displacement y of the upper interface with time t for different initial weight fractions of water, w_i. Only every fifth datapoint is plotted in figure 3a to avoid overcrowding the plot. The datapoints are the average of at least three independent experimental realizations, while the errorbars (± one standard deviation) reflect the uncertainty due to experimental variations and the resolution of the imaging. The velocity $v_y = \mathrm{d}y/\mathrm{d}t$ of the top interface, calculated from y, is plotted as discrete datapoints in figure 3b.

The motion of the top interface obviously depends on the initial composition of the liquid mixture (figure 3 and Supplementary Video V1). For pure water ($w_i = 1$), the interface moves at an almost constant velocity ($y = v_y\, t$ and $v_y \approx 10^{-3}\mathrm{mm\,s^{-1}}$, see figure 3). For $w_i = 0.2$ and 0.6, the experiments suggest $y \sim t^{1/2}$ and $v_y \sim t^{-1/2}$ scaling relations. However, for $w_i = 0.9$, the experiments show three different regimes: $v_y \approx 0.8 \times 10^{-3}\mathrm{mm\,s^{-1}}$, similar to $w_i = 1$, in the first ≈ 800 seconds; $v_y \sim t^{-1/2}$, similar

to $w_i = 0.2$ and 0.6, at intermediate times (up to around $t < 5 \times 10^4$ seconds); and a decrease in velocity (which is steeper than $v_y \sim t^{-1/2}$) at long times.

The addition of glycerol primarily reduces the local concentration of water at the lower interface, which in turn leads to a reduced evaporation rate and a decrease in the velocity of the upper interface. Thus, we get the so-called constant rate period and the so-called falling rate period as described in literature (Salmon *et al.* 2017). Our experimental results, however, raise several important questions. Firstly, why does the constant rate period not appear for $w_i = 0.2$ and 0.6 in the experiments? Secondly, why does the falling rate period show two sub-regimes for $w_i = 0.9$? To answer these questions and to understand how the evaporation dynamics of a water-glycerol mixture in a capillary change with time and with the initial composition of the mixture, we develop a theoretical model in the following section.

3. Problem formulation

3.1. *Theoretical model*

We model the column of water-glycerol mixture as a one-dimensional isothermal system with length $L(t)$ (figure 2b). The lower end of the capillary is located at $z = 0$. We can express the composition using the weight fraction of water $w(z, t)$; the weight fraction of glycerol then simply is $1 - w(z, t)$. The spatio-temporal variations in the concentration of water in the liquid column can be determined by solving the one-dimensional continuity equation and the one-dimensional advection-diffusion equation:

$$\frac{\partial \rho}{\partial t} + \frac{\partial}{\partial z}(\rho\, u) = 0 \tag{3.1}$$

and

$$\frac{\partial}{\partial t}(\rho\, w) + u\, \frac{\partial}{\partial z}(\rho\, w) = \frac{\partial}{\partial z}\left(\rho\, D\, \frac{\partial w}{\partial z}\right), \tag{3.2}$$

where $\rho(w)$ is the local density of the mixture, $D(w)$ the diffusion coefficient of water-glycerol mixture, and u the fluid velocity along the z-direction.

Initially ($t = 0$), the composition in the liquid column is uniform and equal to w_i. Since the evaporation of water from the upper interface is negligible (see appendix A), we model the upper interface to be a non-evaporative surface. The lower interface of the liquid column is exposed to the ambient at a constant relative humidity of H_r and loses water by evaporation (per unit area) at the rate $\mathrm{d}M''/\mathrm{d}t$. The water lost to evaporation is replenished by the diffusive and advective transport of water from the bulk liquid inside the capillary. These considerations lead to the following boundary conditions:

$$\begin{aligned} w &= w_i && \text{at} \quad t = 0, \\ \frac{\partial w}{\partial z} &= 0 && \text{at} \quad z = L(t), \\ -\rho\, u\, w + \rho\, D\, \frac{\partial w}{\partial z} &= \frac{\mathrm{d}M''}{\mathrm{d}t} && \text{at} \quad z = 0. \end{aligned} \tag{3.3}$$

The evaporation of water from the bottom interface can be approximated using a quasi-steady diffusion-limited model of evaporation of a pinned sessile droplet having zero contact angle (Popov 2005; Stauber *et al.* 2014):

$$\frac{\mathrm{d}M''}{\mathrm{d}t} = \pi\, D_{v,a}\, R\, (c_{w,s} - c_{w,\infty})\, f(\theta_{\mathrm{drop}})\, \frac{1}{\pi\, R^2}, \tag{3.4}$$

where $D_{v,a}$ is the diffusion coefficient of water vapour in air, R the radius of the capillary tube, $c_{w,s}$ the concentration (vapour mass per volume) of water vapour in the air at the lower interface, $c_{w,\infty} = H_r c^o_{w,s}$ the concentration of water vapour in the ambient air (far away from the capillary), $c^o_{w,s}$ the saturation concentration of water vapour at the surface of pure water, θ_{drop} the angle between the horizontal plane and the liquid-air interface at the contact line, and $f(\theta_{\text{drop}})$ a known function of θ_{drop}. For $\theta_{\text{drop}} = 0$ as in our model here, $f(\theta_{\text{drop}}) = 4/\pi$ (Popov 2005; Stauber *et al.* 2014). Thus,

$$\frac{\mathrm{d}M''}{\mathrm{d}t} = \frac{4D_{v,a}}{\pi R}\,(c_{w,s} - c_{w,\infty}). \tag{3.5}$$

$c_{w,s}$ depends on the composition of the liquid mixture close to the interface (at $z = 0^+$) and is given by Raoult's Law as

$$c_{w,s} = a\, c^o_{w,s} = x_o\, \psi_o\, c^o_{w,s}, \tag{3.6}$$

where $a(w)$ is the thermodynamic activity of water, x_o the mole fraction of water in the liquid at $z = 0^+$, and $\psi_o(x_o)$ the activity coefficient of water corresponding to x_o. As long as $c_{w,s} > c_{w,\infty}$, water evaporates from the lower interface.

3.2. *Numerical solution*

We numerically solve the one-dimensional theoretical model that was just described, by using Finite Element Methods simulations with an initial length of $L = 20\,\text{mm}$, to obtain the evaporation rates and the spatio-temporal distribution of the concentration of water w in the capillary. To that end, a line mesh initially consisting of 100 second order Lagrangian elements is created to cover the initial length L. The motion of the top interface is realized by moving the mesh nodes along with the top interface, i.e. by an arbitrary Lagrangian-Eulerian method (ALE) with a Laplace-smoothed mesh. The mesh displacement at the top interface $z = L(t)$, i.e. $\dot{L}(t) = u(L,t)$, is enforced by a Lagrange multiplier acting on the node position at the top. Likewise, the evaporation at the bottom is considered, but here the Lagrange multiplier is acting on the velocity u at $z = 0$, whereas the bottom node remains fixed at $z = 0$.

The implementation of (3.2) and (3.1) along with the boundary conditions (3.3) and (3.5) is achieved by the conventional weak formulations of advection-diffusion equations, including the ALE corrections for the time derivatives. *A posteriori* spatial adaptivity based on the jumps in the slopes of w across the elements is considered. Also, *a posteriori* temporal adaptivity is considered by calculating the difference between the freshly calculated value of each field at each point and its prediction. For the prediction, values from the previous time-steps are extrapolated to the current time. If the difference is large, this means that the system changes excessively during a time step. In that case, the current time step is rejected and calculations are made again with a smaller time-step. The implementation has been done by the finite element library OOMPH-LIB by Heil & Hazel (2006), which monolithically solves the coupled equations with a backward differentiation formula of second order for the temporal integration.

The variation of the diffusion coefficient D as function of the local composition w is considered in the simulations based on the experimental data of D'Errico *et al.* (2004), while the mass density ρ was fitted according to the data of Takamura *et al.* (2012). The activity coefficient of water was calculated by AIOMFAC (Zuend *et al.* 2011). Note that later in this article, i.e. in § 4.2, the variation of these physical properties with the composition will be disregarded in the simulations for the pure purpose of a better comparison with the successively improved analytical considerations.

The results of the direct numerical simulations are shown by the continuous lines in

figure 3. Excellent agreement between the experiments and the numerical simulations is observed. In particular, figure 3b shows that the simulations can reproduce the experimentally observed $v_y \sim t^{-1/2}$ scaling for $w_i = 0.2$ and 0.6, and all the three velocity regimes for $w_i = 0.9$. Interestingly, the simulations also show that for very early times, v_y is almost constant for $w_i = 0.2$ and 0.6 as well. However, we cannot access these time scales in experiments due to limitations arising from the lack of spatio-temporal resolution. Overall, the quantitative match between experiments and numerical simulations show that our theoretical model incorporates all the relevant physics of the problem. In the next section, we will use additional simplifying assumptions to formulate a simplistic model which captures the essential physics of the system and recovers the various evaporation regimes.

4. Analytical model

Our one-dimensional analytical model relies on the following assumptions:
(i) Constant properties: we assume that the properties of the water-glycerol mixture, namely, density ρ and diffusion coefficient D, are constant and equal to the values corresponding to the initial composition. Setting density as constant in the continuity equation (3.1) yields that u is independent of z and only depends on t. Hence,

$$u(z,t) = -v_y(t). \tag{4.1}$$

(ii) Linearisation of the water vapour concentration difference: the concentration of water vapour at the liquid-gas interface depends on the concentration of water at $z = 0^+$ (3.6). To solve the model analytically, we linearise the expression for the difference in concentration of the water vapour between $c_{w,s}(w_i)$ and $c_{w,s}(w_{eq})$ in terms of w (in (3.5)) as

$$c_{w,s} - c_{w,\infty} = c^0_{w,s}\,\frac{x_i\,\psi_i - H_r}{w_i - w_{eq}}\,(w|_{z=0} - w_{eq}), \tag{4.2}$$

where x_i, ψ_i, and w_i are the initial mole fraction, activity coefficient, and weight fraction of water in the liquid mixture, respectively, and w_{eq} the weight fraction of water at equilibrium, *i.e.* when $c_{w,s}$ becomes equal to $c_{w,\infty}$ and evaporation stops. In (4.2), we have effectively linearised $(c_{w,s} - c_{w,\infty})$ in terms of w, between the initial $(w = w_i)$ and final $(w = w_{eq})$ concentration of water. Combining (3.5) and (4.2), we get

$$\frac{\mathrm{d}M''}{\mathrm{d}t} = h^*\,(w|_{z=0} - w_{eq}), \tag{4.3}$$

where h^*, defined as

$$h^* = \frac{4D_{v,a}}{\pi\,R}\,c^0_{w,s}\,\frac{x_i\,\psi_i - H_r}{w_i - w_{eq}}, \tag{4.4}$$

is a modified mass transfer coefficient. We put an asterisk in h^* to denote that its units $(\mathrm{kg\,m^{-2}\,s^{-1}})$ are different from those of the conventional mass transfer coefficient h, which is related to h^* as $h = h^*/\rho$ (unit of $\mathrm{m\,s^{-1}}$).
(iii) Velocity of meniscus: The velocity v_y of the meniscus is related to the mass transfer rate through the following relations:

$$\frac{\mathrm{d}M''}{\mathrm{d}t} = \frac{\mathrm{d}}{\mathrm{d}t}\int_{z=0}^{z=L} \rho w\,\mathrm{d}z\,, \tag{4.5}$$

$$\frac{\mathrm{d}M''}{\mathrm{d}t} = \rho|_{z=L}\,w|_{z=L}\,v_y + \int_{z=0}^{z=L}\frac{\partial}{\partial t}(\rho w)\,\mathrm{d}z. \tag{4.6}$$

We will assume that (4.6) can be approximated, similar to the exact expression (2.1), as

$$v_y = \frac{1}{\rho_w}\frac{\mathrm{d}M''}{\mathrm{d}t}\,. \tag{4.7}$$

We define a diffusive length scale l_D based on the mass transfer coefficient by considering a balance between evaporation and diffusion at the lower interface ((3.3) and (4.3)) as

$$l_D = \frac{D}{h}. \tag{4.8}$$

Based on the aforementioned considerations, we non-dimensionalise the variables as follows:

$$\tilde{w} = \frac{w - w_i}{w_{eq} - w_i}, \quad \tilde{t} = \frac{t}{l_D^2/D} = \frac{h^2\,t}{D}, \quad \tilde{z} = \frac{z}{l_D} = \frac{h\,z}{D}, \quad \tilde{L} = \frac{L}{l_D} = \frac{h\,L}{D}. \tag{4.9}$$

Further, since the velocity of the interface is in fact a proxy for the mass transfer (evaporation) rate of water, we can describe the system in terms of the Sherwood number (Sh, denoting non-dimensional velocity or non-dimensional mass transfer rate):

$$Sh = \frac{\rho_w\, v_y}{h^*(w_i - w_{eq})} \tag{4.10}$$

Substituting (4.1)-(4.9) into (3.2), (3.1), and (3.3), we get the following system of equations, and initial and boundary conditions:

$$\frac{\partial \tilde{w}}{\partial \tilde{t}} - \alpha\,\frac{\partial \tilde{w}}{\partial \tilde{z}} = \frac{\partial^2 \tilde{w}}{\partial \tilde{z}^2}, \tag{4.11}$$

$$\begin{aligned} \tilde{w} &= 0 && \text{at} \quad \tilde{t} = 0, \\ \frac{\partial \tilde{w}}{\partial \tilde{z}} &= 0 && \text{at} \quad \tilde{z} = \tilde{L}, \\ \frac{\partial \tilde{w}}{\partial \tilde{z}} - (1-\alpha)\,\tilde{w} + \beta &= 0 && \text{at} \quad \tilde{z} = 0\,. \end{aligned} \tag{4.12}$$

Here α is the Peclet number of the problem, defined as

$$\alpha = \frac{v_y l_D}{D} = \frac{v_y}{h} \tag{4.13}$$

and

$$\beta = 1 - \frac{\rho\, v_y\, w_i}{h^*(w_i - w_{eq})} = 1 - \alpha\frac{w_i}{w_i - w_{eq}}\,. \tag{4.14}$$

Finally, for the case of pure water, we do not need to solve the model for the binary mixture, since there is no change in the concentration. The velocity of the interface can then be directly obtained by substituting $w_i = 1$ in (4.3):

$$v_y = \frac{4D_{v,a}}{\pi\, R\, \rho_w}\, c^0_{w,s}\,(1 - H_r)\,. \tag{4.15}$$

4.1. *Semi-infinite transient diffusion model*

As the zeroth order simplification, we assume that the advection is negligibly small. Further, we approximate the liquid column as a semi-infinite medium. Thus, the governing equation and the initial and boundary conditions ((4.11) and (4.12)) can be reduced

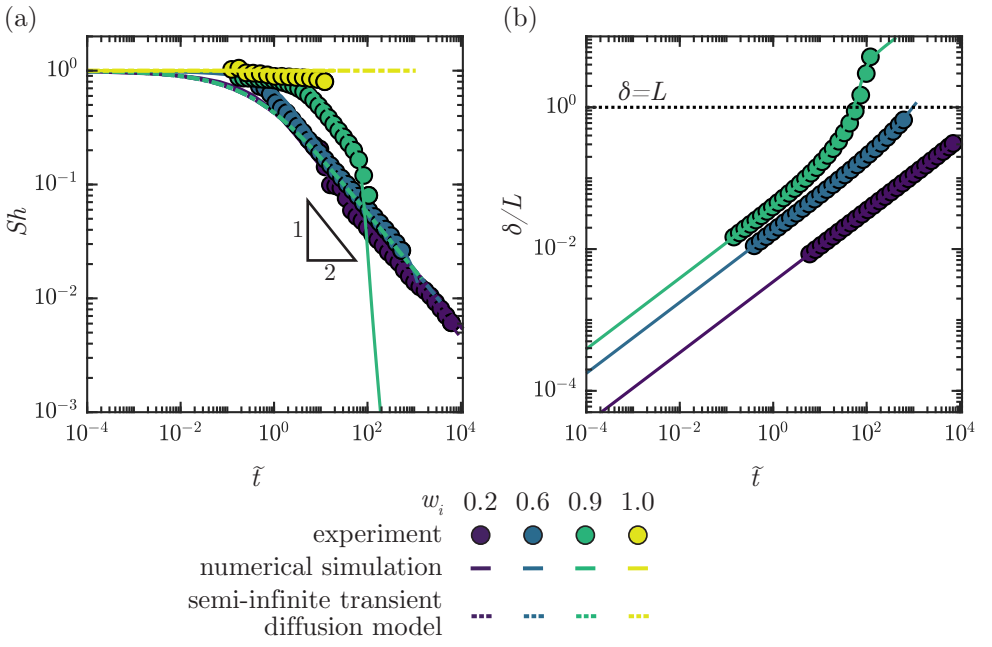

FIGURE 4. (a) Comparison of the normalised evaporation rates (Sherwood number, Sh) against normalised time ($\tilde{t}$) obtained from experiments (discrete datapoints) and numerical simulations (continuous lines) with theoretical values (dashed lines) obtained using the semi-infinite transient diffusion model. (b) Variation of the size of the penetration depth (normalised with the length of the liquid column) with the normalised time ($\tilde{t}$).

to:

$$\frac{\partial \tilde{w}}{\partial \tilde{t}} = \frac{\partial^2 \tilde{w}}{\partial \tilde{z}^2}, \tag{4.16}$$

with

$$\begin{aligned} \tilde{w} &= 0 \qquad \text{at} \quad \tilde{t} = 0, \\ \frac{\partial \tilde{w}}{\partial \tilde{z}} &= 0 \qquad \text{at} \quad \tilde{z} \to \infty, \\ \frac{\partial \tilde{w}}{\partial \tilde{z}} &= \tilde{w} - 1 \qquad \text{at} \quad \tilde{z} = 0. \end{aligned} \tag{4.17}$$

This is a classical transient diffusion problem with mixed boundary condition, whose solution is given by Incropera *et al.* (2007):

$$\tilde{w}\left(\tilde{z}, \tilde{t}\right) = \operatorname{erfc}\left(\frac{\tilde{z}}{2\sqrt{\tilde{t}}}\right) - \exp\left(\tilde{t} + \tilde{z}\right) \operatorname{erfc}\left(\frac{\tilde{z}}{2\sqrt{\tilde{t}}} + \sqrt{\tilde{t}}\right). \tag{4.18}$$

The velocity of the top interface can be now evaluated from the evaporation rate of water (using (4.7), (4.3), and (4.18)) to yield

$$v_y = \frac{h^*(w_i - w_{eq})}{\rho_w} \exp(\tilde{t}) \operatorname{erfc}\left(\sqrt{\tilde{t}}\right), \tag{4.19}$$

or

$$Sh = \exp\left(\tilde{t}\right) \operatorname{erfc}\left(\sqrt{\tilde{t}}\right). \tag{4.20}$$

For $\tilde{t} \to 0$, $Sh \to 1$, whereas for $\tilde{t} \gg 1$, $Sh \approx 1/\sqrt{\pi \tilde{t}}$.

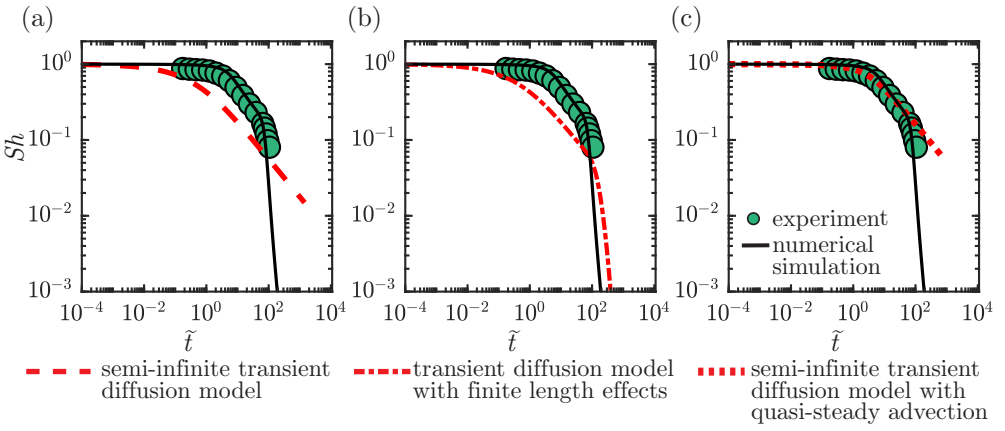

FIGURE 5. Plots comparing the normalised evaporation rates (Sherwood number, Sh) versus normalised time ($\tilde{t}$) obtained from experiments (discrete datapoints) and numerical simulations (continuous lines) with theoretical values obtained using the (a) semi-infinite transient diffusion model (dashed line), (b) transient diffusion model with finite length effects (dash-dotted line), and (c) semi-infinite transient diffusion model with quasi-steady advection (dotted line) for initial weight fraction of water $w_i = 0.9$.

The predictions of the semi-infinite transient diffusion model (4.20) are compared in figure 4a with the experimental measurements (discrete datapoints) and the numerical simulations (continuous lines). It can be observed that (4.20) correctly predicts the early time limit of $Sh = 1$ for all cases, and $Sh \sim 1/\sqrt{\tilde{t}}$ at intermediate times for $w_i = 0.2$ and 0.6. Furthermore, figure 4a also shows that the predicted value of Sh from the model agrees reasonably well with the experiments and the simulations for $w_i = 0.2$ and 0.6. However, (4.20) severely underpredicts the Sherwood number for $w_i = 0.9$ until $\tilde{t} \approx 80$. Moreover, (4.20) also fails to capture the steep decay in Sh seen in the simulations for $w_i = 0.9$ at long times (figure 5a). This calls for a careful re-examination of the assumptions made in the model, starting with the semi-infinite assumption.

For the semi-infinite assumption to hold, the penetration depth of the diffusion front $\delta(t) = \sqrt{Dt}$ should be much smaller than the length of the liquid column $L(t)$. We plot the variation of δ/L with $\tilde{t}$ as obtained from the experiments and numerical simulations in figure 4b for different w_i. It can be observed that for $w_i = 0.9$, $\delta/L = 1$ at $\tilde{t} \approx 60$, which approximately agrees with the time when the slope of $Sh\,(\tilde{t})$ starts to deviate from $Sh \sim \tilde{t}^{-1/2}$. Thus we conclude that although the semi-infinite assumption holds at early times, finite length effects should be included at later times for $w_i = 0.9$ to accurately capture the physics of the problem.

4.2. *Transient diffusion model with finite length effects*

To include the effects of the finite length, we use the original boundary conditions of (3.3).We note that, for early times, since the penetration depth of the diffusion front $\delta(t)$ is much smaller than the length of the liquid column $L(t)$, the changes in L do not affect the evaporation rate significantly. Further, at later times, since $\mathrm{d}L/\mathrm{d}t$ is small, changes in L are slow enough to not affect $w|_{z=0}$ (and consequently the evaporation rate, based on (4.3)). Moreover, we still do not consider the effect of advection. Thus, we formulate a quasi-constant-length transient diffusion model.

In the non-dimensional space, the governing equations, and the initial and boundary

conditions can now be written as

$$\frac{\partial \tilde{w}}{\partial \tilde{t}} = \frac{\partial^2 \tilde{w}}{\partial \tilde{z}^2}, \tag{4.21}$$

$$\begin{aligned} \tilde{w} &= 0 \qquad \text{at} \quad \tilde{t} = 0, \\ \frac{\partial \tilde{w}}{\partial \tilde{z}} &= 0 \qquad \text{at} \quad \tilde{z} = \tilde{L}, \\ \frac{\partial \tilde{w}}{\partial \tilde{z}} &= \tilde{w} - 1 \qquad \text{at} \quad \tilde{z} = 0. \end{aligned} \tag{4.22}$$

The solution of this system of equations is given by (Crank 1975):

$$\tilde{w}(\tilde{z}, \tilde{t}, \tilde{L}) = 1 - \sum_{n=1}^{\infty} \left(\frac{2\tilde{L} \cos\left(\beta_n \left(1 - \tilde{z}/\tilde{L}\right)\right) \exp\left(-\beta_n^2 \, \tilde{t}/\tilde{L}^2\right)}{\left(\beta_n^2 + \tilde{L}^2 + \tilde{L}\right) \cos(\beta_n)} \right), \tag{4.23}$$

where β_n is the n^{th} root of the equation $\beta \tan(\beta) = \tilde{L}$. The velocity of the top interface can be written as

$$\frac{\mathrm{d}L}{\mathrm{d}t} = v_y = \frac{h^*(w_i - w_{eq})}{\rho_w} \sum_{n=1}^{\infty} \frac{2\tilde{L} \exp\left(-\beta_n^2 \, \tilde{t}/\tilde{L}^2\right)}{\left(\beta_n^2 + \tilde{L}^2 + \tilde{L}\right) \cos(\beta_n)}, \tag{4.24}$$

or

$$Sh = \sum_{n=1}^{\infty} \frac{2\tilde{L} \exp\left(-\beta_n^2 \, \tilde{t}/\tilde{L}^2\right)}{\left(\beta_n^2 + \tilde{L}^2 + \tilde{L}\right) \cos(\beta_n)}. \tag{4.25}$$

Equation (4.24) is integrated in time using the built-in Matlab function `ode45` (which implements an adaptive-time-step Runge-Kutta algorithm of fourth order) to obtain $L(t)$, and subsequently the variation of the Sherwood number Sh with the normalised time $\tilde{t}$ (figure 5b). For $\tilde{t} \to \infty$, v_y can be approximated by the first term in the series:

$$v_y = \frac{h^*(w_i - w_{eq})}{\rho_w} \frac{2\tilde{L} \exp\left(-\beta_1^2 \, \tilde{t}/\tilde{L}^2\right)}{\left(\beta_1^2 + \tilde{L}^2 + \tilde{L}\right) \cos(\beta_1)}. \tag{4.26}$$

When the change in length L of the liquid column is small, the velocity decreases exponentially with time (4.26), thus correctly predicting the late time $v(t)$ behaviour of $w_i = 0.9$ (figure 5b). Thus this model captures all the three regimes of evaporation, i.e. the regimes of $Sh(\tilde{t})$, as observed in the experiments and simulations.

However, figure 5b indicates that there is still a difference in the predicted values of Sherwood number between the model and the actual values obtained from experiments and simulations. In particular, (4.25) still severely underpredicts the Sherwood number for $w_i = 0.9$ until $\tilde{t} \approx 80$ (figure 5b). It is not clear *a priori* whether the transient diffusion and finite length effects are sufficient to explain the whole phenomenon. We need to test whether the remaining deviations in the theoretical model simply originate from the assumptions of a linear concentration difference (4.2) and constant properties of the mixture. To answer this question, we can impose the approximations that were used in the analytical model in the numerical simulations as well, and see if the predictions from the simulation match the analytical model.

Figure 6 shows the weight fraction of water at the lower interface, as obtained in the idealised simulations (black solid line) and in the analytical model (red dash-dotted

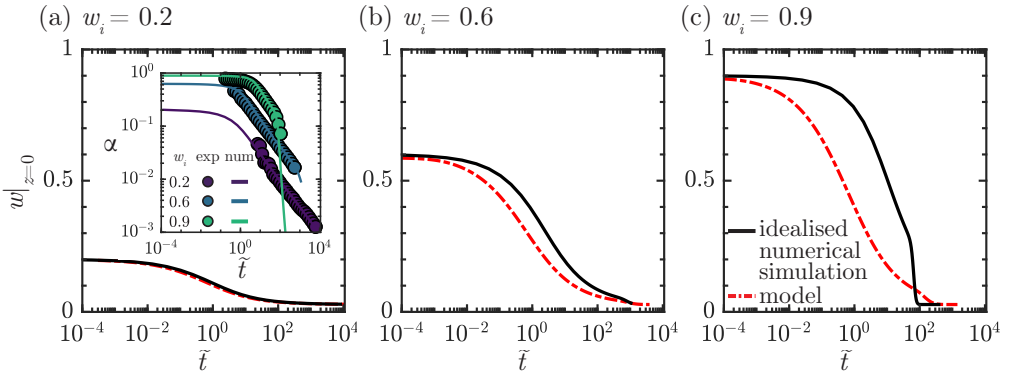

FIGURE 6. Plots comparing the normalised mass transfer rates of idealised numerical simulations and the quasi constant-length model, where the largest deviation is observed for $w_i = 0.9$.

line) for three different initial concentrations. It can be observed that even with the simplifications of constant material properties and linearised concentration difference, the weight fraction of water at the lower interface is much higher in the idealised simulations as compared to the analytical model. This difference leads to a higher mass transfer rate in the simulations as compared to the analytical model (according to (4.3)).

The biggest difference between the idealised simulation and the analytical model is the presence of advection in the numerical simulation. In the idealised simulations shown in figure 6, both advection and diffusion contribute to the replenishment of the water that was lost to evaporation at the liquid boundary $z = 0$. On the contrary, in the analytical model thus far, water is replenished at the lower interface only by diffusion. Therefore, we hypothesise that the difference between the simulations and the analytical model is mainly due to the presence of advection in the simulations which was disregarded in the simplistic analytical model.

To estimate the significance of advection quantitatively, we turn our attention to the advective term, proportional to the Peclet number α, in the non-dimensional governing equation (4.11).

As can be observed from the inset of figure 6a, α is large for high w_i and at initial times, suggesting that to accurately predict the evaporation rates in these situations, the advective contribution to the mass transfer process should be included in the analytical model as well.

4.3. *Semi-infinite transient diffusion model with quasi-steady advection*

To quantitatively predict the evaporation including the effect of advection, we propose an improvement over our simplistic analytical model. However, to avoid combining the effects of finite length and advection, we will model our system as a semi-infinite medium while including advection. Further, we assume that the changes in velocity are slow, such that it can be considered quasi-steady for the purpose of analysis. Thus, we develop a transient diffusion model with quasi-steady advection.

We use the full form of equation (4.11) with the initial and boundary conditions given in (3.3), except that we modify the boundary condition at $\tilde{z} = \tilde{L}$ to

$$\frac{\partial \tilde{w}}{\partial \tilde{z}} = 0 \qquad \text{at} \qquad \tilde{z} \to \infty, \tag{4.27}$$

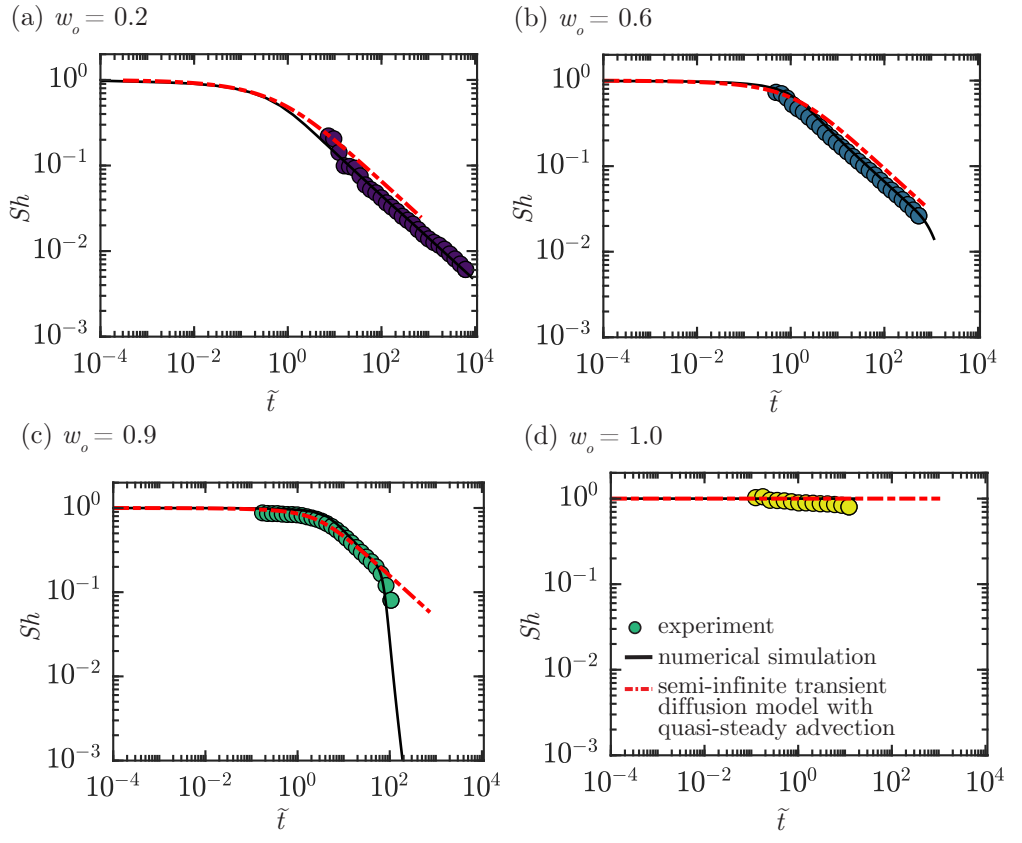

FIGURE 7. Variation of the normalised evaporation rates (Sherwood number, Sh) with normalised time ($\tilde{t}$) obtained from experiments (discrete datapoints) and numerical simulations (continuous lines) with theoretical values (dashed lines) obtained using semi-infinite transient diffusion model with quasi-steady advection, for different initial weight fractions of water w_i.

Solving the system of equations (see appendix B), we get

$$Sh = 1 - \beta \left(1 + \frac{\alpha}{2(1-\alpha)} \operatorname{erfc}\left(\frac{\alpha\sqrt{\tilde{t}}}{2} \right) - \frac{2-\alpha}{2(1-\alpha)} \exp\left((1-\alpha)\tilde{t}\right) \operatorname{erfc}\left(\left(1 - \frac{\alpha}{2}\right)\sqrt{\tilde{t}} \right) \right). \tag{4.28}$$

In the early time limit ($\tilde{t} \to 0$) we get $Sh \to 1$. Similarly, in the late time limit ($\tilde{t} \to \infty$), the velocities are very low. Thus, as the Peclet numner $\alpha \to 0$, we get $\beta \to 1$ and $Sh \to \exp\left(\tilde{t}\right) \operatorname{erfc}\left(\sqrt{\tilde{t}}\right)$, which is the result obtained for pure diffusion. Thus, for $\tilde{t} \to \infty$, we get $Sh \to \exp\left(\tilde{t}\right) \operatorname{erfc}\left(\sqrt{\tilde{t}}\right) \approx 1/\sqrt{\pi\tilde{t}}$. Hence, the quasi-steady advection model recovers the scaling laws for early time and late time limits observed in the experiments and simulations. The results of the quasi constant-advection transient diffusion model are shown in figure 7, indicating a better quantitative agreement with experiments and full numerical simulations. Thus, the model recovers the relevant scaling laws and also provides a better quantitative agreement with the experiments and simulations.

5. Conclusions and outlook

In this work, we studied the evaporation of aqueous glycerol solutions in capillaries with a circular cross section. We characterised the drying behaviour in terms of a normalised mass transfer rate (Sherwood number Sh) and a normalised time $\tilde{t}$. Time is normalised with a diffusive time scale based on mass transfer coefficient. Our experiments quantitatively show how the addition of glycerol reduces the evaporation rate of water. The corresponding direct numerical simulations indicate that modelling the system as a one-dimensional advection-diffusion mass transfer problem with composition-dependent properties can quantitatively reproduce the evaporation behaviour observed in the experiments. The evaporation of water shows three main regimes: (a) $Sh = 1$, (b) $Sh \sim 1/\sqrt{\tilde{t}}$, and (c) $Sh \sim \exp\left(-\tilde{t}\right)$. We describe the physical origins of these regimes using a one-dimensional simplistic analytical model with constant material properties and a linearised composition-dependent activity of water.

Modelling the system as a problem of pure diffusion in a semi-infinite medium reproduces $Sh = 1$ and $Sh \sim 1/\sqrt{\tilde{t}}$ as the early time and late time behaviours, respectively. $Sh = 1$ in the early-time limit corresponds to a rapid replenishment of water at the evaporating interface, leading to a constant evaporation rate and constant interfacial concentration of water. In the late time regime, replenishment of the interfacial concentration of water is limited by diffusion, leading to the classical diffusion-like $Sh \sim 1/\sqrt{\tilde{t}}$ behaviour. However, as the diffusive penetration depth $\delta = \sqrt{Dt}$ increases and the length $L(t)$ of the system decreases, they can become similar in magnitude. In such a scenario, the late time behaviour is modified to $Sh \sim \exp(-\tilde{t})$. This change in the evaporation regime essentially reflects the effect of the finite size of the liquid column.

Finally, we show that even if the pure diffusion model captures the scaling relations of $Sh(\tilde{t})$ correctly, advective replenishment of water needs to be considered for precise prediction of the evaporation rates. A Peclet number defined as $\alpha = \rho v_y / h^* = (w|_{z=0} - w_{eq})\rho/\rho_w$, is the relevant parameter dictating the importance of advection. Thus, advection is small when the interfacial concentration of water $w|_{z=0}$ is close to the equilibrium concentration w_{eq}, and high otherwise.

Even though a model with constant material properties was used to describe the evaporation of a binary mixture, the spatio-temporal changes in properties such as the density and the diffusion coefficient affect the precise quantitative prediction of evaporation rates. The direct numerical simulations are devoid of these deficiencies. However, the simplified analytical models provide insight into the essential physics of the system and can provide predictions for more complex liquid mixtures.

We also note that for predicting the evaporation rate, we have used the expression corresponding to a thin droplet on a substrate ($\theta_{\text{drop}} = 0°$), giving excellent predictions that match the experimental observations. However, one can include corrections to the mass transfer coefficient h^* to account for the difference between the air-liquid interface of a droplet and the air-liquid interface at the mouth of a capillary tube (Li *et al.* 2019). Furthermore, during evaporation, the shape of the lower interface changes ($\theta < 90°$), until the meniscus depins. This change in the shape of the interface might also require a small correction to h^*, and might explain the very small decrease in Sherwood number seen in experiments of pure water (figure 3 b). However, further studies are required in this direction, along the lines of D'Ambrosio *et al.* (2021).

Finally, all measurements were limited to the time when the lower meniscus was pinned to the mouth of the capillary. When the lower meniscus depins and propagates into the capillary, the rate-limiting step of evaporation would change from 3-D vapour diffusion to 1-D vapour diffusion. In the case of a single component liquid evaporating

from a square capillary, there have been efforts to predict the time when the lower meniscus depins (Chauvet *et al.* 2010). Further studies are required to predict the same for multi-component liquids and capillaries of various geometries and configurations (*e.g.* inclination with respect to gravity).

Porous structures and membranes can be modelled as a bundle of thin tubes. Thus these results can be directly applied to predict the evaporation of multi-component liquids from porous structures. Evaporation from capillaries can also help us to understand the evaporative behaviour of biological fluids (such as blood, saliva or liquids in respiratory droplets (Seyfert *et al.* 2022; Merhi *et al.* 2022)) or novel liquid mixtures (for applications such as evaporative cooling and spray drying). Lastly, studying evaporation from capillaries can also be useful in the case of inkjet printing, where the evaporation from the tip of the printing nozzle can lead to changes in the composition of the ink (Rump *et al.* 2022). Our model can give insight into the changes in the composition at the nozzle tip for a given time scale and assist in carefully choosing the properties of the ink.

Acknowledgments

The authors thank Andrea Prosperetti for insightful discussions, and Martin Bos, Gert-Wim Bruggert, Dennis van Gils, and Thomas Zijlstra for their assistance with the fabrication of the controlled humidity chamber.

Funding

We acknowledge the funding by an Industrial Partnership Programme of the Netherlands Organisation for Scientific Research (NWO), co-financed by Canon Production Printing B. V., University of Twente, and Eindhoven University of Technology. D.L. acknowledges funding by the ERC Advanced Grant No. 740479-DDD. J.R.R. acknowledges funding from the Spanish MCIN/AEI/10.13039/501100011033 through grant no. PID2020-114945RB-C21. X.H.Z. acknowledges the support by the Natural Sciences and Engineering Research Council of Canada (NSERC), Alberta Innovates, and the support from the Canada Research Chairs program.

Declaration of interests

The authors report no conflict of interest.

Supplementary information

Supplementary information is available at (URL to be inserted by publisher).

Author ORCID

L. Thayyil Raju https://orcid.org/0000-0002-2054-3884;
C. Diddens https://orcid.org/0000-0003-2395-9911;
J. Rodríguez-Rodríguez https://orcid.org/0000-0001-8181-138X;
X. Zhang https://orcid.org/0000-0001-6093-5324
D. Lohse https://orcid.org/0000-0003-4138-2255;
U. Sen https://orcid.org/0000-0001-6355-7605 .

Appendix A. Evaporation from the upper interface

The evaporative flux from the top interface is given by (Stefan 1873):

$$\frac{\mathrm{d}M''}{\mathrm{d}t} = \frac{D_{v,a}}{L}\frac{p}{RT}\ln\left(\frac{p - p_{w,L}}{p - p_{w,s}}\right), \tag{A 1}$$

where p is the atmospheric pressure, $p_{w,s}$ the partial pressure of water vapour at the surface of the upper meniscus, $p_{w,L}$ the partial pressure of water vapour at the upper end of the capillary tube, and L the length of the capillary tube above the upper meniscus. Since $p_{w,s}$ is much smaller than p, the above expression can be simplified as

$$\frac{\mathrm{d}M''}{\mathrm{d}t} = \frac{D_{v,a}}{L}\left(\frac{p_{w,s}}{RT} - \frac{p_{w,L}}{RT}\right) = \frac{D_{v,a}}{L}\left(c_{w,s} - c_{w,L}\right). \tag{A 2}$$

Thus the ratio of evaporative flux from the top interface to the bottom interface can be estimated as

$$\frac{\frac{\mathrm{d}M''_{\mathrm{top}}}{\mathrm{d}t}}{\frac{\mathrm{d}M''_{\mathrm{bottom}}}{\mathrm{d}t}} = \frac{\frac{D_{v,a}}{L}\left(c_{w,s} - c_{w,L}\right)_{\mathrm{top}}}{\frac{4D_{v,a}}{\pi R}\left(c_{w,s} - c_{w,L}\right)_{\mathrm{bottom}}} \tag{A 3}$$

Thus, even if the top of the capillary is subjected to the same humidity as the bottom, the evaporation from the top is lower by a factor of $\frac{\pi R}{4L} = 0.005$. Hence, the evaporation from the upper interface can be neglected.

Appendix B. Derivation of semi-infinite transient diffusion model with quasi-steady advection

We start with the Laplace transform of (4.11), (4.12), and (4.27), to obtain

$$s\hat{w} - \tilde{w}(\tilde{t}=0) - \alpha\frac{\partial \hat{w}}{\partial \tilde{z}} = \frac{\partial^2 \hat{w}}{\partial \tilde{z}^2}, \tag{B 1}$$

$$\begin{aligned} \frac{\partial \hat{w}}{\partial \tilde{z}} &= 0 \qquad && \text{at} \quad \tilde{z} \to \infty, \\ \frac{\partial \hat{w}}{\partial \tilde{z}} - (1-\alpha)\hat{w} + \frac{\beta}{s} &= 0 \qquad && \text{at} \quad \tilde{z} = 0, \end{aligned} \tag{B 2}$$

where $\hat{w}$ is the Laplace transform of $\tilde{w}$ and s is the variable in the Laplace domain. Solving this system of equations, we get

$$\hat{w} = \frac{-\beta}{s}\frac{1}{\frac{\alpha}{2} - 1 - \sqrt{s + \frac{\alpha^2}{4}}}\exp\left(-\frac{\alpha\tilde{z}}{2} - \tilde{z}\sqrt{\frac{\alpha^2}{4} + s}\right). \tag{B 3}$$

Taking the inverse Laplace transform, we arrive at

$$L^{-1}\left[\hat{w}\right] = \tilde{w} = \beta\exp\left(\frac{-\alpha\tilde{z}}{2}\right) L^{-1}\left[\frac{1}{s}\frac{1}{\frac{\alpha}{2} - 1 - \sqrt{s + \frac{\alpha^2}{4}}}\exp\left(-\tilde{z}\sqrt{\frac{\alpha^2}{4} + s}\right)\right]. \tag{B 4}$$

Using the identity

$$L^{-1}[F(s-\zeta)] = \exp(\zeta)L^{-1}F(s), \tag{B 5}$$

with $\zeta = -\alpha^2/4$, we obtain

$$\tilde{w} = \beta\,\exp\left(\frac{-\alpha\tilde{z}}{2}\right)\exp\left(\frac{-\alpha^2\tilde{t}}{4}\right) L^{-1}\left[\frac{1}{s - \frac{\alpha^2}{4}}\frac{1}{1 - \frac{\alpha}{2} + \sqrt{s}}\exp\left(-\tilde{z}\sqrt{s}\right)\right]. \tag{B 6}$$

Further, we can write (van Genuchten & Alves 1982)

$$L^{-1}\left(\exp\left[\frac{-x\sqrt{s}}{(s-\mu^2)(\xi+s)}\right]\right) = \frac{C}{2(\mu+\xi)} - \frac{D}{2(\mu-\xi)} + E, \tag{B 7}$$

where

$$C = \exp(\mu^2 t - \mu x)\,\mathrm{erfc}\left(\frac{x}{2\sqrt{t}} - \mu\sqrt{t}\right), \tag{B 8}$$

$$D = \exp(\mu^2 t + \mu x)\,\mathrm{erfc}\left(\frac{x}{2\sqrt{t}} + \mu\sqrt{t}\right), \tag{B 9}$$

and

$$E = \frac{\xi}{\mu^2 - \xi^2}\,\exp(\xi^2 t + \xi x)\,\mathrm{erfc}\left(\frac{x}{2\sqrt{t}} + \xi\sqrt{t}\right), \tag{B 10}$$

where having $\mu = \alpha/2$ and $\xi = 1 - \alpha/2$, we get

$$\tilde{w} = F + G + H, \tag{B 11}$$

where

$$F = \frac{\beta}{2}\exp(-\alpha\tilde{z})\mathrm{erfc}\left(\frac{\tilde{z}}{2\sqrt{\tilde{t}}} - \frac{\alpha\sqrt{\tilde{t}}}{2}\right), \tag{B 12}$$

$$G = -\frac{\beta}{2(\alpha-1)}\mathrm{erfc}\left(\frac{\tilde{z}}{2\sqrt{\tilde{t}}} + \frac{\alpha\sqrt{\tilde{t}}}{2}\right), \tag{B 13}$$

and

$$H = \frac{\beta}{2}\frac{2-\alpha}{\alpha-1}\,\exp\left((1-\alpha)\tilde{t}\right)\,\exp\left((1-\alpha)\tilde{z}\right)\,\mathrm{erfc}\left(\frac{\tilde{z}}{2\sqrt{\tilde{t}}} + \left(1 - \frac{\alpha}{2}\right)\sqrt{\tilde{t}}\right). \tag{B 14}$$

Combining with (4.10), we finally obtain

$$Sh = 1 - \beta\left(1 + \frac{\alpha}{2(1-\alpha)}\mathrm{erfc}\left(\frac{\alpha\sqrt{\tilde{t}}}{2}\right) - \frac{2-\alpha}{2(1-\alpha)}\exp((1-\alpha)\tilde{t})\,\mathrm{erfc}\left(\left(1 - \frac{\alpha}{2}\right)\sqrt{\tilde{t}}\right)\right). \tag{B 15}$$

REFERENCES

Abkarian, M., Nunes, J. & Stone, H. A. 2004 Colloidal Crystallization and Banding in a Cylindrical Geometry. *J. Am. Chem. Soc.* **126** (19), 5978–5979.

Bacchin, P, Leng, J & Salmon, J-B 2022 Microfluidic Evaporation, Pervaporation, and Osmosis: From Passive Pumping to Solute Concentration. *Chem. Review* **122** (7), 6938–6985.

Bennacer, R. & Sefiane, K. 2014 Vortices, dissipation and flow transition in volatile binary drops. *J. Fluid Mech.* **749**, 649–665.

Bourouiba, L. 2021 The fluid dynamics of disease transmission. *Annu. Rev. Fluid Mech.* **53**, 473–508.

Buffone, C. 2019 How external buoyancy controls the Marangoni convection for a volatile meniscus inside a pore. *Int. J. Therm. Sci.* **138**, 605–611.

Buffone, C. & Sefiane, K. 2003 Marangoni Convection in Capillary Tubes Filled With Volatile Liquids. *International Conference on Nanochannels, Microchannels, and Minichannels*, vol. Proceedings of the ASME 2003 1st International Conference on Microchannels and Minichannels, pp. 651–657.

Camassel, B., Sghaier, N., Prat, M. & Nasrallah, S. B. 2005 Evaporation in a capillary tube of square cross-section: application to ion transport. *Chem. Eng. Sci.* **60** (3), 815–826.

Cecere, A., Buffone, C. & Savino, R. 2014 Self-induced Marangoni flow in evaporating alcoholic solutions. *Int. J. Heat Mass Transfer* **78**, 852–859.

Chauvet, F., Duru, P., Geoffroy, S. & Prat, M. 2009 Three Periods of Drying of a Single Square Capillary Tube. *Phys. Rev. Lett.* **103** (12), 124502.

Chauvet, F., Duru, P. & Prat, M. 2010 Depinning of evaporating liquid films in square capillary tubes: Influence of corners' roundedness. *Phys. Fluids* **22** (11), 112113.

Chen, L., He, A, Zhao, J., Kang, Q., Li, Z-Y, Carmeliet, Jan, Shikazono, Naoki & Tao, Wen-Quan 2022 Pore-scale modeling of complex transport phenomena in porous media. *Prog. Energy Combust. Sci.* **88**, 100968.

Chen, X., Ye, H., Fan, X., Ren, T. & Zhang, G. 2016 A review of small heat pipes for electronics. *Appl. Therm. Eng.* **96**, 1–17.

Christy, J.R.E., Hamamoto, Y. & Sefiane, K. 2011 Flow transition within an evaporating binary mixture sessile drop. *Phys. Rev. Lett.* **106** (20), 1–4.

Coussot, P. 2000 Scaling approach of the convective drying of a porous medium. *Eur. Phys. J. B* **15** (3), 557–566.

Crank, J 1975 *The mathematics of Diffusion*. Oxford University Press.

Lopez de la Cruz, Ricardo Arturo, Diddens, Christian, Zhang, Xuehua & Lohse, Detlef 2021 Marangoni instability triggered by selective evaporation of a binary liquid inside a hele-shaw cell. *Journal of Fluid Mechanics* **923**, A16.

D'Ambrosio, H.-M., Colosimo, T., Duffy, B. R., Wilson, S. K., Yang, L., Bain, C. D. & Walker, D. E. 2021 Evaporation of a thin droplet in a shallow well: theory and experiment. *J. Fluid Mech.* **927**, A43.

De Gennes, P. G. 2001 Instabilities during the evaporation of a film: Non-glassy polymer+ volatile solvent. *Eur. Phys. J. E* **6** (1), 421–424.

Deegan, R. D., Bakajin, O., Dupont, T. F., Huber, G., Nagel, S. R. & Witten, T. A. 1997 Capillary flow as the cause of ring stains from dried liquid drops. *Nature* **389** (6653), 827–829.

D'Errico, Gerardino, Ortona, Ornella, Capuano, Fabio & Vitagliano, Vincenzo 2004 Diffusion Coefficients for the Binary System Glycerol + Water at 25 °C. A Velocity Correlation Study. *J. Chem. Eng. Data* **49** (6), 1665–1670.

Dhavaleswarapu, H. K., Chamarthy, P., Garimella, S. V. & Murthy, J. Y. 2007 Experimental investigation of steady buoyant-thermocapillary convection near an evaporating meniscus. *Phys. Fluids* **19** (8), 082103.

Dhavaleswarapu, H. K., Murthy, J. Y. & Garimella, S. V. 2012 Numerical investigation of an evaporating meniscus in a channel. *Int. J. Heat Mass Transfer* **55** (4), 915–924.

Diddens, Christian 2017 Detailed finite element method modeling of evaporating multi-component droplets. *J. Comput. Phys.* **340**, 670–687.

Diddens, C., Tan, H., Lv, P., Versluis, M., Kuerten, J. G.M., Zhang, X. & Lohse, D. 2017 Evaporating pure, binary and ternary droplets: Thermal effects and axial symmetry breaking. *J. Fluid Mech.* **823**, 470–497.

Duursma, G., Sefiane, K. & Clarke, J. 2008 Diffusion-Evaporation Studies of Binary Mixtures in Capillary Tubes. *Defect and Diffusion Forum* **273-276**, 577–582.

Erbil, H. Y. 2012 Evaporation of pure liquid sessile and spherical suspended drops: A review. *Adv. Colloid Interface Sci.* **170** (1-2), 67–86.

Gazzola, D., Franchi Scarselli, E. & Guerrieri, R. 2009 3D visualization of convection patterns in lab-on-chip with open microfluidic outlet. *Microfluid. Nanofluid.* **7** (5), 659.

van Genuchten, M. Th. & Alves, W. J. 1982 Analytical Solutions of the One-Dimensional Convective-Dispersive Solute Transport Equation. Technical Bulletins 1661. United States Department of Agriculture, Economic Research Service.

Guerrier, B., Bouchard, C., Allain, C. & Bénard, C. 1998 Drying kinetics of polymer films. *AIChE Journal* **44** (4), 791–798.

He, F., Wang, Z., Wang, L., Li, J. & Wang, J. 2015 Effects of surfactant on capillary evaporation process with thick films. *Int. J. Heat Mass Transfer* **88**, 406–410.

Heil, Matthias & Hazel, Andrew L. 2006 oomph-lib - An Object-oriented multi-physics finite-element library. *Lecture Notes in Computational Science and Engineering* **53**, 19–49.

Hu, H. & Larson, R. G. 2006 Marangoni effect reverses coffee-ring depositions. *J. Phys. Chem. B* **110** (14), 7090–7094.

Incropera, F. P., Dewitt, D.P., Bergman, T. L. & Lavine, A.S. 2007 *Fundamentals of Heat and Mass Transfer*. John Wiley & Sons.

Kamp, U., Kitaev, V., Von Freymann, G., Ozin, G. A. & Mabury, S. A. 2005 Colloidal crystal capillary columns-towards optical chromatography. *Adv. Mater.* **17** (4), 438–443.

Keita, E., Faure, P., Rodts, S., Coussot, P. & Weitz, D. A 2014 Evaporation From a Capillary Tube : Experiment and Modelisation. *5th International Conference on Porous Media and Their Applications in Science, Engineering and Industry* .

Keita, E., Koehler, S. A., Faure, P., Weitz, D. A. & Coussot, P. 2016 Drying kinetics driven by the shape of the air/water interface in a capillary channel. *Eur. Phys. J. E* **39** (2), 23.

Li, J., Shan, L., Ma, B., Jiang, X., Solomon, A., Iyengar, M., Padilla, J. & Agonafer, D. 2019 Investigation of the confinement effect on the evaporation behavior of a droplet pinned on a micropillar structure. *J. Colloid Interface Sci.* **555**, 583–594.

Li, Y., Diddens, C., Segers, T., Wijshoff, H., Versluis, M. & Lohse, D. 2020 Rayleigh–taylor instability by segregation in an evaporating multicomponent microdroplet. *J. Fluid Mech.* **899**, A22.

Lohse, D. 2022 Fundamental fluid dynamics challenges in inkjet printing. *Annu. Rev. Fluid Mech.* **54**, 349–382.

Lohse, D. & Zhang, X. 2020 Physicochemical hydrodynamics of droplets out of equilibrium. *Nat. Rev. Phys.* **2** (8), 426–443.

Merhi, T., Atasi, O., Coetsier, C., Lalanne, B. & Roger, K. 2022 Assessing suspension and infectivity times of virus-loaded aerosols involved in airborne transmission. *Proceedings of the National Academy of Sciences* **119** (32), e2204593119.

Morris, D. H., Yinda, K. C., Gamble, A., Rossine, F. W., Huang, Q., Bushmaker, T., Fischer, R. J., Matson, M. J., van Doremalen, N., Vieksland, P. J., Marr, L. C., Munster, V. J. & Lloyd-Smith, J. O. 2021 Mechanistic theory predicts the effects of temperature and humidity on inactivation of sars-cov-2 and other enveloped viruses. *eLife* **10**, e65902.

Naillon, A., Duru, P., Marcoux, M. & Prat, M. 2015 Evaporation with sodium chloride crystallization in a capillary tube. *J. Cryst. Growth* **422**, 52–61.

Nguyen, H-T, Bouchaudy, A & Salmon, J-B 2022 Microfluidic free interface diffusion: Measurement of diffusion coefficients and evidence of interfacial-driven transport phenomena. *Phys. Fluids* **34** (5), 052008.

Okazaki, M., Shioda, K., Masuda, K. & Toei, R. 1974 Drying mechanism of coated film of polymer solution. *J. Chem. Eng. Jpn.* **7** (2), 99–105.

Okuzono, T., Ozawa, K. & Doi, M. 2006 Simple Model of Skin Formation Caused by Solvent Evaporation in Polymer Solutions. *Phys. Rev. Lett.* **97** (13), 136103.

Park, K. & Lee, K-S 2003 Flow and heat transfer characteristics of the evaporating extended meniscus in a micro-capillary channel. *Int. J. Heat Mass Transfer* **46** (24), 4587–4594.

Picknett, R.G & Bexon, R. 1977 The evaporation of sessile or pendant drops in still air. *J. Colloid Interface Sci.* **61** (2), 336–350.

Popov, Yuri O. 2005 Evaporative deposition patterns: Spatial dimensions of the deposit. *Phys. Rev. E: Stat., Nonlinear, Soft Matter Phys.* **71** (3), 1–17.

Potash, M & Wayner, P.C 1972 Evaporation from a two-dimensional extended meniscus. *Int. J. Heat Mass Transfer* **15** (10), 1851–1863.

Prat, M. 2002 Recent advances in pore-scale models for drying of porous media. *Chem. Eng. J.* **86** (1), 153–164.

Ransohoff, T.C & Radke, C.J 1988 Laminar flow of a wetting liquid along the corners of a predominantly gas-occupied noncircular pore. *J. Colloid Interface Sci.* **121** (2), 392–401.

Roger, K. & Crassous, J. J. 2021 How the interplay of molecular and colloidal scales controls drying of microgel dispersions. *Proc. Natl. Acad. Sci. U. S. A.* **118** (46).

Roger, K., Liebi, M., Heimdal, J., Pham, Q. D. & Sparr, E. 2016 Controlling water evaporation through self-assembly. *Proc. Natl. Acad. Sci. U. S. A.* **113** (37), 10275–10280.

Roger, K., Sparr, E. & Wennerström, H. 2018 Evaporation, diffusion and self-assembly at drying interfaces. *Phys. Chem. Chem. Phys.* **20** (15), 10430–10438.

Rump, M., Sen, U., Jeurissen, R., Reinten, H., Versluis, M., Lohse, D., Diddens, C. & Segers, T. 2022 Selective evaporation at the nozzle exit in piezoacoustic inkjet printing. *Phys. Rev. Applied* In press. arXiv:2205.06639.

Salmon, J.-B., Doumenc, F. & Guerrier, B. 2017 Humidity-insensitive water evaporation from molecular complex fluids. *Phys. Rev. E* **96**, 032612.

Sarkar, A. & Tirumkudulu, M. S. 2009 Consolidation of charged colloids during drying. *Langmuir* **25** (9), 4945–4953.

Saure, R., Wagner, G.R. & Schlünder, E.-U. 1998 Drying of solvent-borne polymeric coatings: I. Modeling the drying process. *Surf. Coat. Technol.* **99** (3), 253–256.

Schmidt, G. & Chung, T. 1992 *Thermocapillary flow about an evaporating meniscus*. American Institute of Aeronautics and Astronautics.

Sen, U., Sanjay, V. & Lohse, D. 2022 Viscous dissipation dictates the maximum spreading diameter of an impacting droplet. (to be published).

Seyfert, C., Rodríguez-Rodríguez, J., Lohse, D. & Marin, A. 2022 Stability of respiratory-like droplets under evaporation. *Phys. Rev. Fluids* **7**, 023603.

Shahidzadeh-Bonn, N., Rafai, S., Bonn, D. & Wegdam, G. 2008 Salt crystallization during evaporation: Impact of interfacial properties. *Langmuir* **24** (16), 8599–8605.

Shin, S., Jacobi, I. & Stone, H. A. 2016 Bénard-Marangoni instability driven by moisture absorption. *Europhys. Lett.* **113** (2).

Sobac, B. & Brutin, D. 2011 Triple-line behavior and wettability controlled by nanocoated substrates: Influence on sessile drop evaporation. *Langmuir* **27** (24), 14999–15007.

Sparr, E. & Wennerström, H. 2000 Diffusion through a responding lamellar liquid crystal: A model of molecular transport across stratum corneum. *Colloid Surface B* **19** (2), 103–116.

Stauber, J. M., Wilson, S. K., Duffy, B. R. & Sefiane, K. 2014 On the lifetimes of evaporating droplets. *J. Fluid Mech.* **744**, R2.

Stefan, J. 1873 Versuche Über die verdampfung. *Sitzungsber. kais. Akad. Wiss. Wien. Math.* **68**, 385–423.

Stefan, J. 1889 Über die Verdampfung und die Auflösung als Vorgänge der Diffusion. *Sitzungsber. kais. Akad. Wiss. Wien. Math.* **98**, 1418–1442.

Swanson, L. W. & Herdt, G. C. 1992 Model of the Evaporating Meniscus in a Capillary Tube. *J. Heat Transfer* **114** (2), 434–441.

Takamura, Koichi, Fischer, Herbert & Morrow, Norman R. 2012 Physical properties of aqueous glycerol solutions. *J. Pet. Sci. Eng.* **98-99**, 50–60.

Tan, H., Diddens, C., Lv, P., Kuerten, J. G.M., Zhang, X. & Lohse, D. 2016 Evaporation-Triggered microdroplet nucleation and the four life phases of an evaporating Ouzo drop. *Proc. Natl. Acad. Sci. U. S. A.* **113** (31), 8642–8647.

Wang, S., Zhou, H., Sun, Z., Xu, S., Ouyang, W. & Wang, L. 2020 Evolution of concentration and phase structure of colloidal suspensions in a two-ends-open tube during drying process. *Sci. Rep.* **10** (1), 9084.

Wayner, P.C., Kao, Y.K. & LaCroix, L.V. 1976 The interline heat-transfer coefficient of an evaporating wetting film. *Int. J. Heat Mass Transfer* **19** (5), 487–492.

Wayner JR., P. C. & Coccio, C. L. 1971 Heat and mass transfer in the vicinity of the triple interline of a meniscus. *AIChE Journal* **17** (3), 569–574.

Yiotis, A. G., Tsimpanogiannis, I. N., Stubos, A. K. & Yortsos, Y. C. 2007 Coupling between external and internal mass transfer during drying of a porous medium. *Water Resour. Res.* **43** (6).

Zhou, L., Zhou, S., Du, X. & Yang, Y. 2018 Heat transfer characteristics of a binary thin liquid film in a microchannel with constant heat flux boundary condition. *Int. J. Therm. Sci.* **134** (February), 612–621.

Zimmermann, M., Bentley, S., Schmid, H., Hunziker, P. & Delamarche, E. 2005 Continuous flow in open microfluidics using controlled evaporation. *Lab on Chip* **5** (12), 1355–1359.

Zuend, A., Marcolli, C., Booth, A. M., Lienhard, D. M., Soonsin, V., Krieger, U. K., Topping, D. O., McFiggans, G., Peter, T. & Seinfeld, J. H. 2011 New and extended parameterization of the thermodynamic model aiomfac: calculation of activity coefficients for organic-inorganic mixtures containing carboxyl, hydroxyl, carbonyl, ether, ester, alkenyl, alkyl, and aromatic functional groups. *Atmos. Chem. Phys.* **11** (17), 9155–9206.